Neuro-Oncology Advance Access published August 8, 2016

Neuro-Oncology

Neuro-Oncology 2016; **0**, 1–9, doi:10.1093/neuonc/now135

Radiogenomics to characterize regional genetic heterogeneity in glioblastoma

Leland S. Hu†, Shuluo Ning†, Jennifer M. Eschbacher, Leslie C. Baxter, Nathan Gaw, Sara Ranjbar, Jonathan Plasencia, Amylou C. Dueck, Sen Peng, Kris A. Smith, Peter Nakaji, John P. Karis, C. Chad Quarles, Teresa Wu, Joseph C. Loftus, Robert B. Jenkins, Hugues Sicotte, Thomas M. Kollmeyer, Brian P. O'Neill, William Elmquist, Joseph M. Hoxworth, David Frakes, Jann Sarkaria, Kristin R. Swanson, Nhan L. Tran†, Jing Li†, and J. Ross Mitchell†

Department of Radiology, Mayo Clinic, Phoenix, Arizona (L.S.H., T.W., J.M.H.); Department of Biostatistics, Mayo Clinic, Phoenix, Arizona (A.C.D.); Department of Research, Mayo Clinic, Arizona (J.R.M., K.S.); Department of Neurosurgery, Mayo Clinic, Phoenix, Arizona (K.R.S.); Department of Cancer and Cell Biology, Mayo Clinic, Scottsdale, Arizona (J.C.L.); Department of Pathology, Mayo Clinic, Rochester, Minnesota (R.B.J., T.M.K.); Department of Biomedical Statistics and Informatics, Mayo Clinic, Rochester, Minnesota (H.S.); Department of Neuro-oncology, Mayo Clinic, Rochester, Minnesota (B.P.O.); Department of Radiation Oncology, Mayo Clinic, Rochester, Minnesota (J.S.); Department of Pharmaceutics, University of Minnesota, Minneapolis, Minnesota (W.E.); Department of Cancer and Cell Biology, Translational Genomics Research Institute, Phoenix, Arizona (S.P., N.L.T.); School of Computing, Informatics and Decision Systems Engineering, Arizona State University, Tempe, Arizona (J.L., T.W., S.N., N.G.); Department of Biomedical Informatics, Arizona State University, Tempe, Arizona (S.R.); School of Biological and Health Systems Engineering, Arizona State University, Tempe, Arizona (J.P., D.F.); Department of Pathology, Barrow Neurological Institute – St. Joseph's Hospital and Medical Center, Phoenix, Arizona (J.M.E.); Department of Neurosurgery, Barrow Neurological Institute – St. Joseph's Hospital and Medical Center, Phoenix, Arizona (K.A.S., P.N.); Department of Radiology, Barrow Neurological Institute – St. Joseph's Hospital and Medical Center, Phoenix, Arizona (L.C.B., J.P. K., L.S.H.); Department of Imaging Research, Barrow Neurological Institute – St. Joseph's Hospital and Medical Center, Phoenix, Arizona (C.C.Q.)

Corresponding Author: Leland S. Hu, MD., Department of Radiology at Mayo Clinic, Arizona. 5777 E. Mayo Blvd, Phoenix, AZ, 85054 (hu.leland@mayo.edu)

†(contributed equally)

Background. Glioblastoma (GBM) exhibits profound intratumoral genetic heterogeneity. Each tumor comprises multiple genetically distinct clonal populations with different therapeutic sensitivities. This has implications for targeted therapy and genetically informed paradigms. Contrast-enhanced (CE)-MRI and conventional sampling techniques have failed to resolve this heterogeneity, particularly for nonenhancing tumor populations. This study explores the feasibility of using multiparametric MRI and texture analysis to characterize regional genetic heterogeneity throughout MRI-enhancing and nonenhancing tumor segments.

Methods. We collected multiple image-guided biopsies from primary GBM patients throughout regions of enhancement (ENH) and nonenhancing parenchyma (so called brain-around-tumor, [BAT]). For each biopsy, we analyzed DNA copy number variants for core GBM driver genes reported by The Cancer Genome Atlas. We co-registered biopsy locations with MRI and texture maps to correlate regional genetic status with spatially matched imaging measurements. We also built multivariate predictive decision-tree models for each GBM driver gene and validated accuracies using leave-one-out-cross-validation (LOOCV).

Results. We collected 48 biopsies (13 tumors) and identified significant imaging correlations (univariate analysis) for 6 driver genes: *EGFR*, *PDGFRA*, *PTEN*, *CDKN2A*, *RB1*, and *TP53*. Predictive model accuracies (on LOOCV) varied by driver gene of interest. Highest accuracies were observed for *PDGFRA* (77.1%), *EGFR* (75%), *CDKN2A* (87.5%), and *RB1* (87.5%), while lowest accuracy was observed in *TP53* (37.5%). Models for 4 driver genes (*EGFR*, *RB1*, CDKN2A, and *PTEN*) showed higher accuracy in BAT samples ($n = 16$) compared with those from ENH segments ($n = 32$).

Conclusion. MRI and texture analysis can help characterize regional genetic heterogeneity, which offers potential diagnostic value under the paradigm of individualized oncology.

Keywords: genetic, glioblastoma, heterogeneity, radiogenomics, texture.

Received 2 March 2016; accepted 20 May 2016

Glioblastoma (GBM) exhibits broad genetic diversity that contributes to treatment resistance and poor survival. Recent discoveries through genetic profiling have given insight into new strategies for improving outcomes.[1] In particular, the paradigm of individualized oncology selects treatments to match the targetable aberrations within each tumor. While this approach seeks to maximize drug response and patient survival, GBM's intratumoral heterogeneity creates significant challenges.[2] Specifically, each tumor comprises multiple genetically distinct clonal populations (so called "many tumors in one") that can express different therapeutic targets.[3] This renders non-localizing biopsies prone to sampling errors, since genetic profiles from one location may not accurately reflect other subregions. Such errors can misguide treatment, leading to poor or incomplete response.[4] Further, contrast-enhanced MRI (CE-MRI) guides surgical targeting from enhancing regions (ENH), but neglects the clonal populations within the nonenhancing parenchyma (so called "brain around tumor" [BAT]).[5,6] These BAT populations remain unresected and poorly characterized despite representing the primary targets of adjuvant therapy and the main contributors to recurrence.[5,6] These issues underscore the need to better characterize GBM's intratumoral genetic heterogeneity, particularly within the nonenhancing BAT.

As an integral part of clinical practice, MRI can characterize a diverse spectrum of tumoral phenotypes as potential biomarkers of genetic status. For instance, enhancement on CE-MRI correlates with blood brain barrier (BBB) disruption, while T2W/FLAIR abnormalities demarcate tumoral edema in the BAT. Advanced MRI can report other biophysical features such as tumor cell density on diffusion-weighted imaging (DWI),[8] white matter infiltration on diffusion-tensor imaging (DTI),[6,8] and microvessel morphology on perfusion MRI (pMRI).[9,10] In addition, MRI spatially encodes signal intensity values for all voxels comprising each image. The textural patterns between voxel intensities and their surrounding neighbors provide further insight to tissue microstructure and the local environment.[11,12] Numerous studies have correlated both MRI signal and texture analysis with genetic profiles in GBM,[5,11,13–21] yet these have been limited in resolving the challenge of GBM's intratumoral heterogeneity. A major reason is that most groups use nonlocalizing biopsies to determine a single representative profile for an entire tumor.[11,13–21] By definition, this does not account for the genetic diversity throughout the various tumor subregions. Also, most biopsies originate from MRI enhancement per routine surgical practice, so tumor profiles from the nonenhancing BAT are typically under-represented.[5] Thus, particularly for tumors that ultimately receive a gross total resection of MRI enhancement, the molecular targets of the BAT are unknown.

In this exploratory study, we evaluated the feasibility of using multiparametric MRI and texture analysis to characterize the regional genetic heterogeneity throughout the ENH and BAT tumor segments of GBM. To accomplish this, we collected multiple image-guided biopsies throughout both segments in a cohort of patients with primary GBM. For each biopsy, we analyzed genome-wide DNA somatic copy number variants (CNVs) to determine the regional status for highly recurrent and biologically significant GBM driver genes, as previously determined by The Cancer Genome Atlas (TCGA).[1,22] These include known therapeutic targets and core GBM pathways such as receptor tyrosine kinase (RTK), phosphoinositide 3-kinase (PI3K), mitogen-activated protein kinase (MAPK), tumor protein p53 (TP53), and retinoblastoma (RB1). We coregistered each biopsy location with preoperative multiparametric MRI, which includes CE-MRI, DWI, DTI, and pMRI. This allowed us to correlate regional genetic status with spatially matched imaging measurements including raw MRI signal and MRI-based texture features. Finally, we used both univariate and multivariate analyses to determine which MRI-based features correlated most strongly with regional status for each driver gene. Our overarching goal is to develop image-based biomarkers that can improve diagnostic accuracy and treatment selection under the paradigm of individualized oncology.

Methods

Patient Recruitment

We recruited patients with clinically suspected GBM undergoing preoperative stereotactic MRI for surgical resection. We confirmed the absence of previous treatment (including steroid administration). We obtained approval from the institutional review boards and obtained written and informed consent from each participant prior to enrollment.

Surgical Biopsy

Our group used preoperative conventional MRI, including T1-weighted contrast-enhanced (T1 + C) and T2-weighted sequences (T2W), to guide stereotactic biopsies as previously described.[23] In short, each neurosurgeon collected an average of 5–6 tissue specimens from each tumor using stereotactic localization, following the smallest possible diameter craniotomies to minimize brain shift. Neurosurgeons generally selected targets separated by ≥1 cm from both ENH (T1 + C) and nonenhancing BAT (T1 + C,T2W) regions within different poles of the tumor based on clinical feasibility (e.g. accessibility of the target site, overlying vessels, eloquent brain).[23] Neurosurgeons recorded biopsy locations to allow subsequent coregistration with multiparametric MRI datasets. The neurosurgeon visually validated stereotactic imaging locations with corresponding intracranial anatomic landmarks, such as vascular structures and ventricle margins, before recording specimen locations.[23]

Histologic Analysis and Tissue Treatment

Tissue specimens (approximately 125 mg) were flash-frozen in liquid nitrogen in the operating suite within 1–2 minutes of collection and stored in −80°C freezer until subsequent processing. Tissue was retrieved and embedded frozen in optimal cutting temperature (OCT) compound. Tissue was sectioned (4 μm) in −20°C cryostat (Microm-HM-550) utilizing microtome blade, stained with hematoxylin and eosin (H&E), and reviewed by neuropathology to ensure adequate tumor content (≥50%).

Genetic Profiling and Analysis

We performed DNA/RNA isolation and determined copy number variant (CNV) for all tissue samples using array comparative genomic hybridization (aCGH) and exome sequencing as previously published and further detailed in Supplemental Methods.[24–26]

This included application of previously described CNV detection to whole genome long insert sequencing data and exome sequencing.[25]

Copy Number Variant Aberrations of Interest

TCGA has previously identified a set of highly recurrent and biologically significant DNA gains and losses through copy number analysis.[1,22] These CNVs comprise known therapeutic targets and/or core GBM pathways: RTK, PI3K, MAPK, TP53, and RB1.[1,22] For this study, we determined which tumor samples demonstrated aberrations for each CNV. To adequately power image-genetic correlative studies, we proceeded with those CNVs altered in ≥20% of our tumor samples. CNVs such as c-MET amplification on 7q31.2, observed in only one of 48 (2.1%) total samples, were excluded from further analyses.

MRI Protocol, Parametric Maps, and Image Coregistration

Conventional MRI and acquisition conditions

We acquired 3T MRI (Sigma HDx; GE-Healthcare) within one day prior to stereotactic surgery. Conventional MRI and Advanced MRI parameters have been detailed previously.[23] Briefly, we acquired postcontrast T1-weighted (T1 + C) SPGR-IR (TI/TR/TE = 300/6.8/2.8 ms; matrix = 320 × 224; Field of View (FOV) 26 cm; thickness = 2 mm) and T2-weighted (T2W) fast-spin-echo (TR/TE = 5133/78 ms; matrix = 320 × 192; FOV = 26 cm; thickness = 2 mm). We acquired T1 + C images after completing dynamic susceptibility-weighted contrast-enhanced (DSC) perfusion MRI (pMRI) following total Gd-DTPA (gadobenate dimeglumine) dosage of 0.15 mmol/kg as previously described.[23,27]

Diffusion Tensor Imaging (DTI)

We acquired DTI using spin-echo echo-planar imaging (EPI) (TR/TE = 10000/85.2 ms, matrix = 256 × 256; FOV = 30 cm, slice = 3 mm, 25 directions, B = 0,1000). We calculated the following parameters as previously described: isotropic (p) and anisotropic (q) diffusion, mean diffusivity (MD) and fractional anisotrophy (FA).[6,23]

DSC-pMRI

We acquired DSC-pMRI as previously detailed.[23,27] Briefly, we administered preload dose (0.1 mmol/kg) before acquiring DSC, which consisted of gradient-echo (GE)-EPI (TR/TE/FA = 1500 ms/20 ms/60°, matrix = 128 × 128, thickness = 5 mm) for 3 minutes. DSC bolus injection (0.05 mmol/kg) commenced at 45 seconds during DSC. The initial source volume of images from the GE-EPI after the PLD, an image we term EPI + C, was acquired without dummy scans (prior to magnetization equilibrium), and thus is sensitive only to regional variations in proton density and postcontrast T2*W signal. Assuming similar proton density within tumor voxels and because the EPI + C signal intensities are acquired at contrast agent equilibrium, EPI + C reflects variations in tissue cellularity (eg, cell density, shape, size, and distribution) as previously described.[23,28] We performed leakage correction and calculated relative cerebral blood volume (rCBV) using IB Neuro (Imaging Biometrics) as previously detailed.[27]

Image coregistration

We coregistered all image datasets using ITK (www.itk.org) and IB Suite (Imaging Biometrics) as previously detailed.[27] Briefly, we used rigid-body techniques to coregister image datasets with varying matrix sizes and FOVs to a common matrix/FOV (all data were registered to the DTI series). We included the additional step of visual validation by expert neuroradiologist review to ensure the accuracy of image co-registration, which further reduced potential errors. Previous work quantifying misregistration error suggests minimal impact on the accuracy of spatial correlations.[29]

Texture Analysis, Image Processing, and Principal Component Analysis (PCA)

Following image coregistration, all MRI data exhibited uniform voxel size (1.2 × 1.2 × 3 mm) across all MRI contrasts (x,y,z dimensions). We generated regions of interest (ROIs) measuring 8 × 8 × 1 voxels (9.6 × 9.6 × 3 mm) at the locations corresponding to each biopsy site. A board-certified neuroradiologist (L.S.H.) visually inspected all ROIs to ensure accuracy. Prior to texture analysis, we acquired first-order statistics from raw image signals: mean (M) and standard deviation (SD) of gray-level intensities. Next, we mapped intensity values within each ROI onto the range 0–255. This step helped standardize intensities between ROIs and reduced effects of intensity nonuniformity on features extracted during subsequent texture analysis. Next, we performed texture analysis as previously detailed, incorporating 3 separate but complementary texture algorithms[11,12,30,31]: gray level co-occurrence matrix,[29] local binary patterns (LBP),[30] and discrete orthonormal Stockwell transform (DOST).[11,12] In total, we generated 30 texture features for each of 8 total MRI contrasts, which yielded 240 MRI-texture features and 16 raw features (ie, mean and SD for 8 MRI contrasts) for a total of 256 image-based features for each ROI. We then performed PCA and determined principal components (PCs) for respective MRI-texture algorithms (GLCM, LBP, DOST) for each ROI.[23] The PCs for respective MRI-texture features were numbered and correlated individually with genetic status as described below. Texture analysis and PCA are further detailed in Supplemental Methods.

Statistical Analysis of Imaging-Genetic Correlations

To broadly survey the potential associations between imaging and genetics, we first performed a univariate analysis comparing each imaging feature at a time against the status of each CNV (aberrant vs diploid/normal). Specifically, we used a 2-sample *t* test to determine statistically significant differences in image feature values between aberrant and diploid CNV status. Sensitivity analysis included comparison of imaging parameters between aberrant and diploid samples using the chi-square test with adjustment for clustering of biopsies within patients.[32] Results remained highly consistent with the primary results, which did not adjust for clustering (results not shown). We also used the Benjamini & Hochberg (1995) false discovery rate to adjust for multiple testing within each texture feature and mutation.[33] Furthermore, we performed multivariate analysis by fitting decision tree-based models on the image features to assess whether multiple image features could be used in a complementary fashion for predicting CNV status.[34] We developed separate decision-tree models for each CNV of interest. When the sample size allowed (ie, ≥20% of tissue specimens demonstrated a particular CNV aberration), we separated BAT and ENH tumor samples, and developed one decision tree for BAT samples and another decision

Table 1. Selected associations between copy number variant and imaging on univariate analysis

CNV	MRI-texture feature	*P* value	Biophysical correlate
EGFR ++ (7p11)	T2W-DOST*	<.005	Tissue water/edema
	T2W-GLCM*	<.002	
	T2W raw SD*	<.004	
	rCBV-LBP*	<.001	Microvessel volume; angiogenesis
PDGFRA ++ (4q12)	P-DOST*	<.0001	Isotropic diffusion; tumor cell density
	P-GLCM*	<.009	
	EPI+C-DOST	<.014	Cellular density
PTEN – (10q23)	T2W-LBP	<.005	Tissue water/edema
CDKN2A – (9p21.3)	EPI+C-LBP	<.004	Cellular density
RB1 – (13q14)	T1+C-GLCM	<.01	MRI enhancement; BBB disruption
	T2W-DOST	<.03	Tissue water/edema
	T2W raw SD	<.008	
TP53 – (17p13)	P-LBP	<.03	Isotropic diffusion; tumor cell density
	T2W-DOST	<.02	Tissue water/edema

Abbreviations: DOST, discrete orthonormal Stockwell transform; GLCM, gray level co-occurrence matrix; LBP, local binary product; SD, standard deviation of raw MRI signal

Listed are the predominant imaging features that correlated with the status of each copy number variant. Each MRI feature is listed by contrast and texture algorithm. For instance, T2W-DOST corresponds with DOST texture of T2W signal. *P* values are based on univariate analysis. Also listed are the biophysical features associated with corresponding MRI contrasts. ++ denotes amplification; – denotes deletion.

Asterisks (*) denote correlations that showed false discovery rate (FDR) <5% when adjusting for multiple testing.

Table 2. Decision-tree models for predicting copy number variant status

CNV	Tumor segment	CNV prevalence (%)	Decision tree AUC	LOOCV accuracy
EGFR ++ (7p11)	BAT	50% (8/16)	0.94	75%
	ENH	40.6% (13/32)	1.00	71.9%
PDGFRA ++ (4q12)	BAT/ENH	22.9% (9/48)	0.89	77.1%
PTEN – (10q23)	BAT	68.8% (11/16)	0.90	68.8%
	ENH	78.1% (25/32)	1.00	43.8%
CDKN2A – (9p21.3)	BAT	62.5% (10/16)	0.95	87.5%
	ENH	65.6% (21/32)	0.94	59.4%
RB1 – (13q14)	BAT	37.5% (6/16)	0.95	87.5%
	ENH	53.1% (17/32)	1.00	43.8%
TP53 – (17p13)	BAT	31.2% (5/16)	1.00	37.5%
	ENH	37.5% (12/32)	1.00	37.5%

Abbreviations: AUC, area under curve; BAT, "brain around tumor"; CNV, copy number variants; ENH, enhanced; LOOCV, leave-one-out cross-validation

Separate decision-tree models were developed to predict CNV status within tumor sample subgroups (ENH vs BAT) except for *PDGFRA*. The lower prevalence of *PDGFRA* alterations required grouping of ENH and BAT samples to develop a single decision-tree model for CNV status. The prevalence of each CNV is listed as a percentage as well as the number of tissue samples with CNV alteration relative to total samples within each group/subgroup. Decision-tree area under curve (AUC) was determined on receiver operating characteristic (ROC) analysis of the training set. We also report cross validation accuracy for each decision-tree model as determined by LOOCV.

tree for ENH samples. However, if separation of BAT and ENH samples resulted in a small sample size (eg, <20% of tissue samples showed CNV aberration), we combined ENH and BAT samples to develop a single decision-tree. For each decision-tree model, we calculated area under the curve (AUC) on receiver operator characteristic (ROC) analysis to determine the accuracy of the training data. We subsequently validated each model's accuracy for predicting/classifying the CNV status using leave-one-out cross validation (LOOCV). LOOCV is a well-known approach for evaluating the accuracy of a statistical model on unseen data.[11,12,23]

Results

Patient Recruitment and Tissue Samples

We collected a total of 81 tissue specimens from 18 GBM patients. Of these, 48 tissue specimens (16 BAT, 32 ENH) from 13

patients (median = 3 specimens/patient) contained adequate tumoral and/or DNA content for successful aCGH analysis. The majority of biopsies (93.75%) were separated by ≥1 cm. Three biopsies (6.25%) were separated by 6–10 mm from other biopsies in the same patient. In this study, we sought to evaluate the regional intratumoral heterogeneity of genetic profiles as documented through multiple stereotactic biopsies within a single tumor. Due to the heterogeneous nature of GBM tumors and the goals of our study, we considered multiple tissue specimens from the same tumor to be independent observations. This approach has been used in multiple previous studies that used imaging to evaluate intratumoral heterogeneity.[5–10,22,27,35] Sensitivity analysis using chi-square testing further supported the minimal impact on correlations when adjusting for clustering of biopsies within patients.[32]

Copy Number Variant Aberrations of Interest

Of the core GBM pathways reported by TCGA,[1,2,22] CNVs associated with 6 driver genes met inclusion criteria (≥20% prevalence) for further imaging-genetic analyses (Tables 1 and 2). *PTEN* deletion on 10q23 was the most commonly observed genetic alteration (75% of total samples), followed by *CDKN2A* deletion on 9p21.3 (64.5%), *RB1* deletion on 13q14 (47.9%), *EGFR* amplification on 7p11 (43.75%), *TP53* deletion on 17p13 (35.4%), and *PDGFRA* amplification on 4q12 (22.9%). Specimens isolated from 7 of 13 GBM tumors demonstrated heterogeneity in genetic profiles such that at least one of the samples showed different CNV aberration(s) compared with the other samples from the same tumor (Fig. 1). For imaging-genetic correlations, we defined aberrations for *PTEN*, *CDKN2A*, *RB1*, and *TP53* as either homozygous or heterozygous deletions.

Univariate Analyses of Imaging-Genetic Associations

The analysis of DTI metrics (p, q, MD, FA) showed that *P* and q values were equivalent to MD and FA, respectively. For all imaging-genetic correlative studies, we proceeded with the analysis of *P* and q values and also used these to represent MD and FA, respectively. On univariate analysis, CNV status correlated more strongly with MRI texture features than with raw MRI signal intensities (ie, mean and standard deviation), suggesting the added value of texture analysis. Table 1 and Fig. 2 summarize the predominant imaging-genetic correlations. *EGFR* amplification showed highly significant correlations with LBP texture on rCBV maps as well as 3 separate features on T2W imaging: 2 texture-based features (on DOST and GLCM) and SD of raw T2W signal. *PDGFRA* amplification strongly correlated with DOST and GLCM texture on isotropic diffusion (p). Each of these imaging correlations demonstrated false discovery rates (FDR) <5% (Table 1, Fig. 2). *PDGFRA* status also correlated moderately with DOST texture on EPI + C. *CDKN2A* showed highly significant correlation with LBP texture on EPI + C, while *PTEN* correlated strongly with LBP texture on T2W imaging. *RB1* deletion correlated moderately with several imaging features (T2W and T1 + C textures and T2W raw[SD]), while *TP53* deletion showed the weakest imaging correlations compared with all other CNVs.

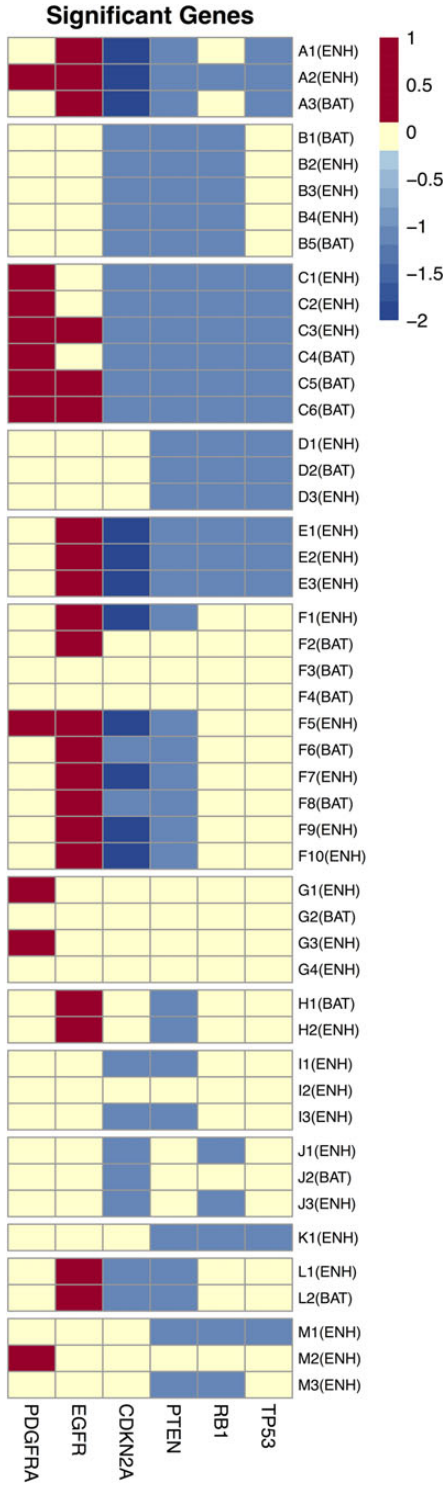

Fig. 1. Copy number variant (CNV) profiles for 48 glioblastoma (GBM) tumor samples from 13 patients. Listed are the tissue samples by patient (eg, A,B,C . . .) and sample number (eg, 1,2,3 . . .). Samples are also demarcated by tumor segment of origin (ENH vs BAT). Red boxes denote amplification, dark blue boxes denote homozygous deletions, light blue boxes denote heterozygous deletions, and yellow boxes denote wild-type status (ie, diploid genome) for respective CNV gene aberrations (listed at the bottom of the x-axis).

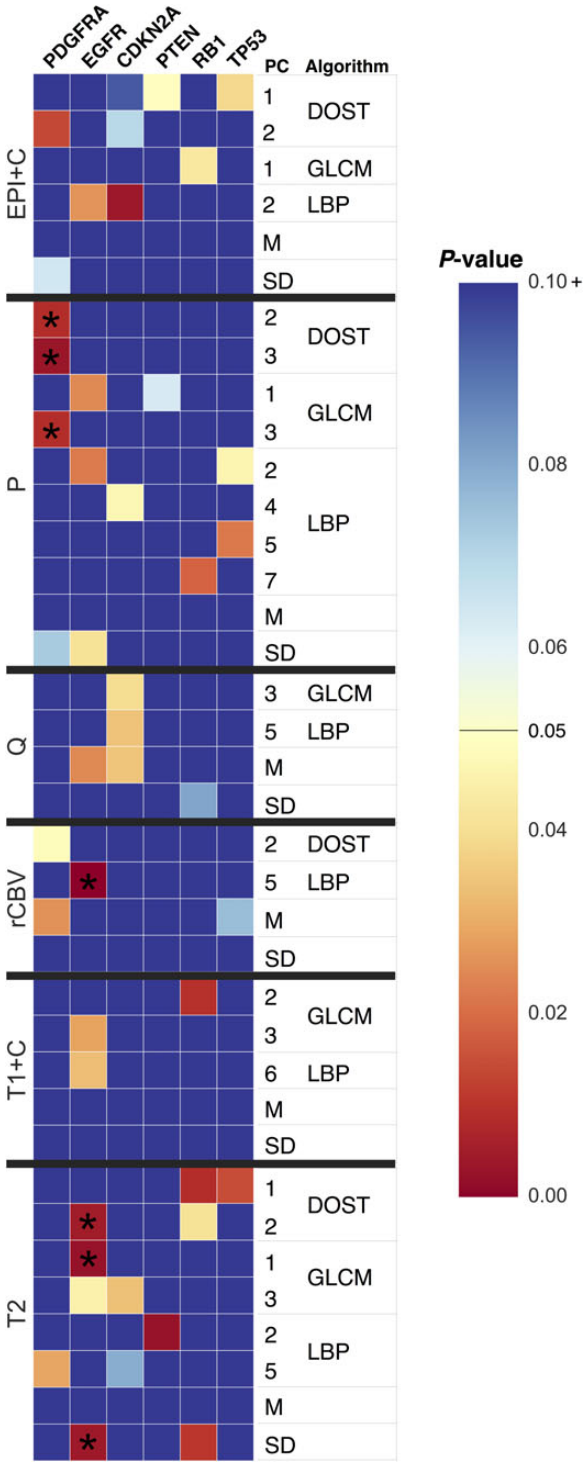

Fig. 2. Heat map showing *P* values for significant imaging correlations with copy number variant (CNV) status. Univariate analysis compared CNV status (aberrant vs diploid/wild-type) with MRI-texture features. CNVs are listed as columns (top). Image features are listed as rows by MRI contrast (left axis) (eg, EPI + C, P, etc) and corresponding texture algorithm (right axis) (ie, DOST, GLCM, LBP). The principal components (PC) that demonstrated statistically significant or trending correlations are listed and labeled numerically (ie, 1,2,3 etc.). Mean (M) and standard deviation (SD) are also listed. Color map shows the *P* values by a 2-sample *t* test. Yellow-to-red colors indicate *P* values ≤.05, while blue signifies *P*values >.05. DOST = discrete-orthonormal-Stockwell-transform; GLCM = gray-level-co-occurrence matrix; LBP = local-binary-product. Asterisks (*) denote correlations with false discovery rate (FDR) <5%.

Multivariate Analysis Through Decision-tree Models and Leave-one-out Cross Validation

Using multivariate analysis, we developed separate decision-tree models for ENH and BAT tumor samples, respectively, for 5 of 6 CNVs of interest. For *PDGFRA*, separating BAT and ENH groups resulted in low prevalence for BAT samples (only 18.75% of samples with amplification). Thus, we grouped BAT and ENH samples to develop one decision-tree model to predict *PDGFRA* amplification. Decision-tree models for all CNVs achieved AUC (Table 2) on the training set, ranging from 0.89 to 1.0. The LOOCV accuracies showed variability depending on the CNV of interest and tumor segment subgroups (BAT vs ENH). Interestingly, 4 of the 6 predictive models showed higher LOOCV accuracies for BAT samples compared with ENH samples: *EGFR* (75% vs 71.9%); *RB1* (87.5% vs 43.8%); *CDKN2A* (87.5% vs 59.4%); *PTEN* (68.8% vs 43.8%). The *PDGFRA* predictive model showed high accuracy (77.1%) in combined BAT/ENH samples. Low LOOCV accuracies were noted in both BAT and ENH samples for *TP53* (37.5% and 37.5%). These LOOCV accuracies are also summarized in Table 2. Tree models are also detailed in Fig. 3 and Supplementary Figs 1–5. A total of 11 tree models were produced. All together these included 25 decision nodes. DOST-based texture features were selected most frequently for tree-model construction (10 of 25 decision nodes), followed by LBP features (7 of 25), GLCM features (7 of 25), and raw features (1 of 25). Supplementary Figs 6 and 7 also show which patient samples contributed to the decision nodes for the EGFR (Supplementary Fig. 6) and PDGFRA (Supplementary Fig. 7) decision-tree models.

Discussion

Previous studies have documented GBM's intratumoral genetic heterogeneity by karyotype,[36] DNA aneuploidy,[37] gene expression profiling[5,35] and, more recently, copy number analysis[1,22,38] and next generation sequencing.[1] This heterogeneity, which is thought to arise from clonal expansion of multiple genetically divergent tumor populations, has implications for targeted therapy and tumoral resistance. Each clonal population can express different drug targets and sensitivities, which promotes the likelihood that pre-existing resistant clones will fail a given therapy and subsequently recur. Neighboring clonal populations can further modulate therapeutic response through biological interactions.[2–4] These issues have motivated recent efforts to develop combinatorial strategies that can overcome and even exploit genetic heterogeneity for therapeutic benefit.[2–4] Also, as genetically informed paradigms become more realistic and feasible, the characterization of intratumoral heterogeneity will play an ever-increasing role in the design of new and effective targeted therapies.

Tissue sampling remains a significant barrier to accurately characterizing intratumoral heterogeneity.[4] While CE-MRI guides surgical biopsies from the enhancing tumor segment

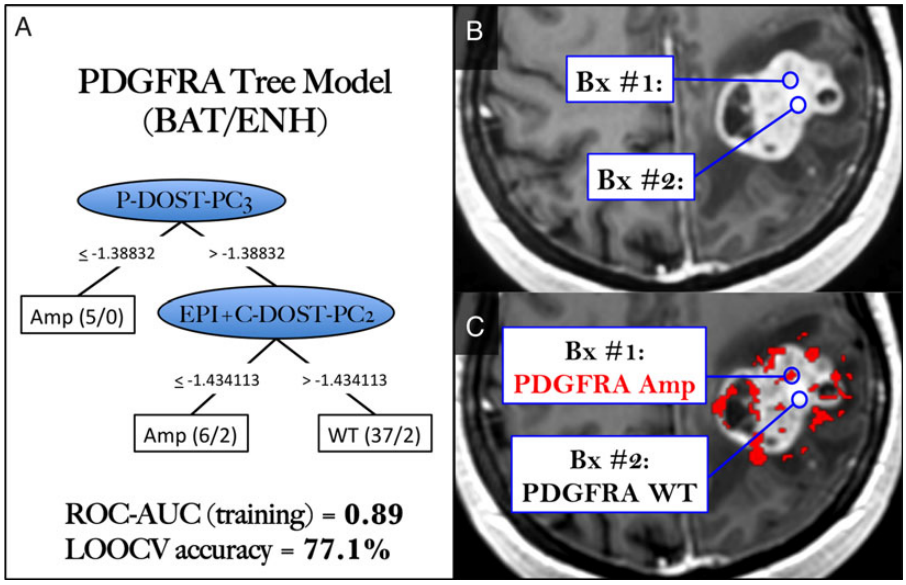

Fig. 3. Decision-tree model for *PDGFRA* copy number variant (CNV) status. (A) Tree model classification for *PDGFRA* amplification was developed through multivariate analysis of CNV status, multiparametric MRI, and texture analysis. The combination of P-DOST and EPI + C-DOST MRI-texture features classifies *PDGFRA* amplified (Amp) and wild-type (WT) specimens, with parentheses denoting (total # classified/# incorrectly classified) specimens at each branch point. Leave-one-out-cross-validation (LOOCV) confirmed 77.1% model accuracy. *P* = isotropic diffusion; EPI + C = T2*W signal loss; DOST = discrete orthonormal Stockwell transform; PC3, PC2 derived from principal component analysis (PCA). (B, C) Shown are the locations of 2 stereotactic biopsies (Bx#1,Bx#2) on CE-MRI. DNA CNVs demonstrated amplification (Amp,Bx#1) and diploid/wild-type status (WT,Bx#2). (C) Color map overlay shows regions (ROIs) of predicted *PDGFRA* amplification (red voxels) using tree model classification. AUC, area under curve.

(ENH), MRI enhancement alone lacks the specificity to resolve the regional and genetically distinct clonal populations throughout each tumor. Numerous correlative studies have evaluated other imaging features as potential biomarkers of genetic status.[5,11,13–21] Yet, most have used nonlocalizing biopsies (typically from a small representative subregion) to determine a single genetic profile for an entire tumor. Unfortunately, this technique fails to inform of intratumoral heterogeneity as a whole since the genetic profiles from one biopsy location may not accurately reflect those from other tumor subregions. In fact, sampling errors can potentially degrade imaging-tissue correlations. Gutman[13] et al. and Jain[14] et al. separately reported the absence of imaging correlations with common putative GBM drivers (eg, *EGFR*, *PDGFRA*, *PTEN*, and *CDKN2A*), which typically show regional heterogeneity throughout each tumor.[22,35] Other studies have reported mixed correlations between whole-tumor imaging and GBM subtypes,[14,16] although these have not accounted for the fact that multiple subtypes can coexist within a single tumor.[22] Meanwhile, different groups using nonlocalizing biopsies have shown conflicting results on whether *EGFR* correlates with perfusion MRI metrics.[14,18–21]

In this study, we collected multiple image-guided biopsies from both ENH and BAT tumor segments to demonstrate intratumoral heterogeneity for core GBM pathways and common therapeutic targets. Although previous studies have shown how tumor samples from nonenhancing BAT can genetically differ from ENH samples,[5,35] our data illustrate that regional genetic diversity can also exist within each tumor segment. This underscores the need to improve the image-based characterization of genetic heterogeneity beyond the use of CE-MRI enhancement alone. While other studies have also used image-guided biopsies,[5,35] our study has taken several unique approaches to facilitate the image-based characterization of regional genetic status including (i) integration of multiple, complementary MRI contrasts, (ii) use of multiple, complementary texture algorithms to probe tissue microstructure and heterogeneity, and (iii) development of predictive models for specific GBM driver genes. These aspects have enabled the identification of multiple, statistically significant associations between localized imaging features and regional CNV status (summarized in Table 1 and Fig. 2).

On univariate analysis, we observed strong correlation between regional EGFR status and LBP texture on rCBV. While mean rCBV quantifies the overall average microvessel volume within a ROI, rCBV texture captures the contributions and signal patterns of the individual voxels within that ROI, giving insight to microvascular distribution and heterogeneity.[5,9,10] Previous studies have investigated the link between *EGFR* and mean rCBV, albeit without localizing biopsies or texture analysis that may explain conflicting results.[14,18–21] Tykocinski[18] et al. and Gupta[19] et al. both found correlations between *EGFR* and raw mean rCBV, while Ryoo[20] et al. and Jain[14] et al. did not. Although sampling error could have contributed to discordance between studies, we used stereotactic biopsies to address this confound and identified no significant correlation between *EGFR* and raw mean rCBV. However, the finding that texture of rCBV correlates with *EGFR* status suggests the benefit of characterizing the regional and intervoxel signal patterns for a particular MRI contrast. *EGFR* also correlated strongly with T2W texture (on DOST and GLCM) as well as T2W intervoxel heterogeneity, as measured by SD of raw signal. The link between *EGFR* and T2W signal patterns of tumoral/vasogenic edema has been suggested previously.[21] The other CNVs also

demonstrated strong correlations with image texture and MRI-based biophysical correlates. *PDGFRA* associated strongly with textures (but not raw mean values) on isotropic diffusion (P-DOST, P-GLCM) and EPI + C measures of cellular density (EPI + C-DOST). Both MRI contrasts have been linked to tumor cell density and proliferation in previous studies.[6–8,23,28] Similarly, *PTEN* and *CDKN2A* correlated highly with textures on T2W (T2W-LBP) and EPI + C (EPI + C-LBP), respectively.

We used multivariate analysis through decision-tree modeling to determine whether MRI-based features, either alone or in combination, could predict CNV status for a given biopsy sample. While all training models achieved high AUC on ROC analysis, cross validation showed that only some models retained high accuracy on LOOCV. For example, the model for *PDGFRA* status (Fig. 3) demonstrated high LOOCV accuracy (77.1%), while model accuracies for *TP53* were low for both BAT and ENH samples. Interestingly, 4 of the 6 models showed noticeably higher LOOCV accuracy for BAT samples compared with ENH samples: *EGFR* (75% vs 71.9%), *RB1* (87.5% vs 43.8%), *CDKN2A* (87.5% vs 59.4%), and *PTEN* (68.8% vs 43.8%). These discrepancies likely relate to multiple underlying factors that warrant further investigation in larger GBM cohorts. One possibility is the influence of driver gene co-expression (eg, *EGFR* and *PTEN*) on image-based phenotypes. Ryoo[20] et al. found that tumors co-expressing *EGFR* amplification and *PTEN* deletion had significantly lower rCBV values compared with tumors having *EGFR* amplification alone (and normal *PTEN* status). Presumably, co-expression of other driver gene combinations could impact a diversity of imaging phenotypes. Future analysis of molecular markers other than DNA gains/losses (eg, epigenetic modulation, mRNA, and proteomic expression) may also help validate or enhance the correlations in this study.[1,2] Finally, further work is needed to evaluate how the image-based characterization of intratumoral heterogeneity might impact clinical decisions about GBM therapy and correlative studies by cooperative initiatives such as TCGA and The Cancer Imaging Atlas (TCIA).[1–5] For instance, quantifying the fraction of tumor populations harboring specific gene alterations could be useful for serially tracking treatment efficacy over time to evaluate how specific tumor regions respond to targeted therapies. This could prove beneficial for proposed strategies such as adaptive therapy,[39] which modulates the selective advantage of the different clonal populations within each tumor to maximize therapeutic benefit. Also, the use of imaging to quantify genetic heterogeneity should enable future comparisons between genetically heterogeneous and homogeneous tumors in regard to differential responses to standard therapy, clinical outcomes, and development of optimal drug regimens to extend survival.

We recognize several limitations to this study. First, given the small sample size of this exploratory study, the tree-model accuracies and univariate analyses need to be prospectively validated in a larger GBM cohort. This should also increase the likelihood of capturing a more diverse set of GBM driver gene alterations (eg, c-MET, CDK4, etc.), which were otherwise too infrequent in our study to adequately characterize by imaging. Prospective validation will also provide the opportunity to integrate these predictive models with surgical neuronavigation, which will facilitate biopsy targeting of genetically diverse regions within each tumor. Second, image distortions and brain shift following craniotomy could lead to misregistration errors. To compensate, neurosurgeons used small craniotomy sizes to minimize brain shift and also visually validated stereotactic image location with intracranial neuroanatomic landmarks to help correct for random brain shifts. Rigid-body coregistration of stereotactic and advanced MR-imaging also helped reduce possible geometric distortions.[5,9,10,23,27] Overall, our experience suggests combined misregistration at approximately 1–2 mm from both brain shift and registration technique, which is similar to that from previous studies using stereotactic needle biopsy.[8] Also, for each patient, we collected multiple tissue samples from spatially distinct subregions within the same tumor. The vast majority of biopsy targets were separated by >1 cm. While approximately 6%–7% of samples (3 out of 48) were separated by 6–10 mm, we used small ROI sizes to minimize the effects of potential sample overlap. We estimate negligible impact from this minority of samples.

Conclusion

This exploratory study uses image-guided biopsies, multiparametric MRI, and texture analysis to establish spatially accurate correlations with regional genetic status for a focused set of common GBM drivers. The results here offer proof of concept that image-based biomarkers can facilitate the characterization of intratumoral genetic heterogeneity. This also provides a framework for future studies to validate these correlations and identify image-based signatures for a broader array of biologically and therapeutically significant genetic alterations in GBM.

Supplementary material

Supplementary material is available at *Neuro-Oncology Journal* online (http://neuro-oncology.oxfordjournals.org/).

Funding

National Institutes of Health (NS082609) (L.S.H.); (CA160045) (J.R.M.); Mayo Clinic Foundation (L.S.H.); National Science Foundation (NSF) Division of Graduate Education (DGE) NSF-DGE-1311230 (J.P.); Barrow Neurolgical Foundation (LCB).

Acknowledgments

We would like to thank Norissa Honea, PhD, and Beth Hermes for their invaluable help with patient recruitment and tissue preparation.

Conflict of interest statement. None declared.

References

1. Brennan CW, Verhaak RG, McKenna A, et al. The somatic genomic landscape of glioblastoma. *Cell*. 2013;155(2):462–477.
2. Bonavia R, Inda MM, Cavenee WK, Furnari FB. Heterogeneity maintenance in glioblastoma: a social network. *Cancer Res*. 2011;71(12):4055–4060.
3. Ene CI, Fine HA. Many tumors in one: a daunting therapeutic prospect. *Cancer Cell*. 2011;20(6):695–697.
4. Marusyk A, Almendro V, Polyak K. Intra-tumour heterogeneity: a looking glass for cancer? *Nat Rev Cancer*. 2012;12(5):323–334.

5. Barajas RF Jr, Hodgson JG, Chang JS, et al. Glioblastoma multiforme regional genetic and cellular expression patterns: influence on anatomic and physiologic MR imaging. *Radiology*. 2010;254(2):564–576.
6. Price SJ, Jena R, Burnet NG, et al. Improved delineation of glioma margins and regions of infiltration with the use of diffusion tensor imaging: an image-guided biopsy study. *AJNR Am J Neuroradiol*. 2006;27(9):1969–1974.
7. Ellingson BM, Malkin MG, Rand SD, et al. Validation of functional diffusion maps (fDMs) as a biomarker for human glioma cellularity. *J Magn Reson Imaging*. 2010;31(3):538–548.
8. Stadlbauer A, Ganslandt O, Buslei R, et al. Gliomas: histopathologic evaluation of changes in directionality and magnitude of water diffusion at diffusion-tensor MR imaging. *Radiology*. 2006;240(3):803–810.
9. Barajas RF Jr, Phillips JJ, Parvataneni R, et al. Regional variation in histopathologic features of tumor specimens from treatment-naive glioblastoma correlates with anatomic and physiologic MR Imaging. *Neuro Oncol*. 2012;14(7):942–954.
10. Hu LS, Eschbacher JM, Dueck AC, et al. Correlations between perfusion MR imaging cerebral blood volume, microvessel quantification, and clinical outcome using stereotactic analysis in recurrent high-grade glioma. *AJNR Am J Neuroradiol*. 2012;33(1):69–76.
11. Brown R, Zlatescu M, Sijben A, et al. The use of magnetic resonance imaging to noninvasively detect genetic signatures in oligodendroglioma. *Clin Cancer Res*. 2008;14(8):2357–2362.
12. Drabycz S, Roldán G, de Robles P, et al. An analysis of image texture, tumor location, and MGMT promoter methylation in glioblastoma using magnetic resonance imaging. *Neuroimage*. 2010;49(2):1398–1405.
13. Gutman DA, Cooper LA, Hwang SN, et al. MR imaging predictors of molecular profile and survival: multi-institutional study of the TCGA glioblastoma data set. *Radiology*. 2013;267(2):560.
14. Jain R, Poisson LM, Gutman D, et al. Outcome prediction in patients with glioblastoma by using imaging, clinical, and genomic biomarkers: focus on the nonenhancing component of the tumor. *Radiology*. 2014;272(2):484–493.
15. Itakura H, Achrol AS, Mitchell LA, et al. Magnetic resonance image features identify glioblastoma phenotypic subtypes with distinct molecular pathway activities. *Sci Transl Med*. 2015;7(303):303ra138.
16. Yang D, Rao G, Martinez J, et al. Evaluation of tumor-derived MRI-texture features for discrimination of molecular subtypes and prediction of 12-month survival status in glioblastoma. *Med Phys*. 2015;42(11):6725–6735.
17. Pope WB, Chen JH, Dong J, et al. Relationship between gene expression and enhancement in glioblastoma multiforme: exploratory DNA microarray analysis. *Radiology*. 2008;249(1):268–277.
18. Tykocinski ES, Grant RA, Kapoor GS, et al. Use of magnetic perfusion-weighted imaging to determine epidermal growth factor receptor variant III expression in glioblastoma. *Neuro Oncol*. 2012;14(5):613–623.
19. Gupta A, Young RJ, Shah AD, et al. Pretreatment Dynamic Susceptibility Contrast MRI Perfusion in Glioblastoma: Prediction of EGFR Gene Amplification. *Clin Neuroradiol*. 2015;25(2):143–150.
20. Ryoo I, Choi SH, Kim JH, et al. Cerebral blood volume calculated by dynamic susceptibility contrast-enhanced perfusion MR imaging: preliminary correlation study with glioblastoma genetic profiles. *PLoS One*. 2013;8(8):e71704.
21. Aghi M, Gaviani P, Henson JW, et al. Magnetic resonance imaging characteristics predict epidermal growth factor receptor amplification status in glioblastoma. *Clin Cancer Res*. 2005;11(24Pt1):8600–8605.
22. Sottoriva A, Spiteri I, Piccirillo SG, et al. Intratumor heterogeneity in human glioblastoma reflects cancer evolutionary dynamics. *Proc Natl Acad Sci USA*. 2013;110(10):4009–4014.
23. Hu LS, Ning S, Eschbacher JM, et al. Multi-parametric MRI and Texture analysis to visualize spatial histologic heterogeneity and tumor extent in glioblastoma. *PLoS One*. 2015;10(11):e0141506.
24. Borad MJ, Champion MD, Egan JB, et al. Integrated genomic characterization reveals novel, therapeutically relevant drug targets in FGFR and EGFR pathways in sporadic intrahepatic cholangiocarcinoma. *PLoS Genet*. 2014;10(2):e1004135.
25. Craig DW, O'Shaughnessy JA, Kiefer JA, et al. Genome and transcriptome sequencing in prospective metastatic triple-negative breast cancer uncovers therapeutic vulnerabilities. *Mol Cancer Ther*. 2013;12(1):104–116.
26. Lipson D, Aumann Y, Ben-Dor A, et al. Efficient calculation of interval scores for DNA copy number data analysis. *J Comput Biol*. 2006;13(2):215–228.
27. Hu LS, Eschbacher JM, Heiserman JE, et al. Reevaluating the imaging definition of tumor progression: perfusion MRI quantifies recurrent glioblastoma tumor fraction, pseudoprogression, and radiation necrosis to predict survival. *Neuro Oncol*. 2012;14(7):919–930.
28. Semmineh NB, Xu J, Skinner JT, et al. Assessing tumor cytoarchitecture using multiecho DSC-MRI derived measures of the transverse relaxivity at tracer equilibrium (TRATE). *Magn Reson Med*. 2015;74(3):772–784.
29. Urish KL, Williams AA, Durkin JR, Chu CR; the OAI Investigators Group. Registration of magnetic resonance image series for knee articular cartilage analysis: data from the osteoarthritis initiative. *Cartilage*. 2013;4(1):20–27.
30. Haralick RM, Karthikeyan S, Dinstein IH. Textural features for image classification. *IEEE Trans Syst Man Cybern*. 1973;6:610–621.
31. Ojala T, Pietikainen M, Maenpaa T. Multiresolution gray-scale and rotation invariant texture classification with local binary patterns. *IEEE Trans Pattern Anal Mach Intell*. 2002;24(7):971–987.
32. Gönen M, Panageas KS, Larson SM. Statistical issues in analysis of diagnostic imaging experiments with multiple observations per patient. *Radiology*. 2001;221(3):763–767.
33. Benjamini Y, Hochberg Y. Controlling the false discovery rate: a practical and powerful approach to multiple testing. *J R Statist Soc B*. 1995;57:289–300.
34. Rokach L, Maimon O. *Data mining with decision trees: theory and applications*. 2014.
35. Van Meter T, Dumur C, Hafez N, et al. Microarray analysis of MRI-defined tissue samples in glioblastoma reveals differences in regional expression of therapeutic targets. *Diagn Mol Pathol*. 2006;15(4):195–205.
36. Shapiro JR, Yung WK, Shapiro WR. Isolation, karyotype, and clonal growth of heterogeneous subpopulations of human malignant gliomas. *Cancer Res*. 1981;41:2349–2359.
37. Coons SW, Johnson PC. Regional heterogeneity in the DNA content of human gliomas. *Cancer*. 1993;72(10):3052–3060.
38. Snuderl M, Fazlollahi L, Le LP, et al. Mosaic amplification of multiple receptor tyrosine kinase genes in glioblastoma. *Cancer Cell*. 2011;20(6):810–817.
39. Gatenby RA, Silva AS, Gillies RJ, Frieden BR. Adaptive therapy. *Cancer Res*. 2009;69:4894–4903.